

On-chip interrogator based on Fourier transform spectroscopy

Peternella, Fellipe Grillo; Esselink, Thomas; Dorsman, Bas; Harmsma, Peter; Horsten, Roland C.; Zuidwijk, Thim; Urbach, H. Paul; Adam, Aurèle L.C.

DOI

[10.1364/OE.27.015456](https://doi.org/10.1364/OE.27.015456)

Publication date

2019

Document Version

Final published version

Published in

Optics Express

Citation (APA)

Peternella, F. G., Esselink, T., Dorsman, B., Harmsma, P., Horsten, R. C., Zuidwijk, T., Urbach, H. P., & Adam, A. L. C. (2019). On-chip interrogator based on Fourier transform spectroscopy. *Optics Express*, 27(11), 15456-15473. <https://doi.org/10.1364/OE.27.015456>

Important note

To cite this publication, please use the final published version (if applicable).
Please check the document version above.

Copyright

Other than for strictly personal use, it is not permitted to download, forward or distribute the text or part of it, without the consent of the author(s) and/or copyright holder(s), unless the work is under an open content license such as Creative Commons.

Takedown policy

Please contact us and provide details if you believe this document breaches copyrights.
We will remove access to the work immediately and investigate your claim.



On-chip interrogator based on Fourier transform spectroscopy

FELIPE GRILLO PETERNELLA,^{1,*} THOMAS ESSELINK,² BAS DORSMAN,¹ PETER HARMSMA,³ ROLAND C. HORSTEN,¹ THIM ZUIDWIJK,¹ H. PAUL URBACH,¹ AND AURÈLE L. C. ADAM¹

¹ *ImPhysics department, TU Delft, Mekelweg 5, 2628 CD Delft, The Netherlands*

² *The Hague University of Applied Sciences, Rotterdamseweg 137, 2628 AL Delft, The Netherlands*

³ *TNO, Mekelweg 5, 2628 CD Delft, The Netherlands*

**F.GrilloPernella@tudelft.nl*

Abstract: In this paper, the design and the characterization of a novel interrogator based on integrated Fourier transform (FT) spectroscopy is presented. To the best of our knowledge, this is the first integrated FT spectrometer used for the interrogation of photonic sensors. It consists of a planar spatial heterodyne spectrometer, which is implemented using an array of Mach-Zehnder interferometers (MZIs) with different optical path differences. Each MZI employs a 3×3 multi-mode interferometer, allowing the retrieval of the complex Fourier coefficients. We derive a system of non-linear equations whose solution, which is obtained numerically from Newton's method, gives the modulation of the sensor's resonances as a function of time. By taking one of the sensors as a reference, to which no external excitation is applied and its temperature is kept constant, about 92% of the thermal induced phase drift of the integrated MZIs has been compensated. The minimum modulation amplitude that is obtained experimentally is 400 fm, which is more than two orders of magnitude smaller than the FT spectrometer resolution.

© 2019 Optical Society of America under the terms of the [OSA Open Access Publishing Agreement](#)

1. Introduction

Photonic based sensors find nowadays a wide range of applications. Acoustic and ultrasound sensors [1, 2], pressure sensors [3], biochemical and gas sensors [4, 5] are examples of sensors based on optical technology. They are low cost, immune to electromagnetic radiation, and operate under a wide range of temperatures. In this paper, we focus our attention on photonic sensors whose transmission or reflection spectra have a peak (or dip) in their lineshape. Examples are sensors based on fiber Bragg gratings (FBGs) [5, 6] or on integrated ring resonators [1, 2, 4]. For these sensors, it is possible to build large and multi-purpose sensor arrays by wavelength multiplexing the spectrum of the sensors [6, 7].

The photonic sensors mentioned above are designed in such a way that the signal to be sensed modulates the sensor's resonance wavelength. Interrogation is the technique of demodulating and demultiplexing the response of an array of photonic sensors. Different methods have been proposed in the past. A common approach is to measure the spectrum of the sensor array using a dispersive spectrometer such as an arrayed waveguide grating (AWG) [8–10] or an echelle grating [11]. Their sensitivity to the external excitation depends on the spectral resolution of the spectrometer; higher resolution comes at the price of a larger footprint. Another approach is edge filtering, where the output spectra of the photonic sensors is conveyed to an optical filter whose transfer function is linear within certain range. As the spectrum of the sensor shifts due to the sensing signal, the filter converts the resonance wavelength modulation into power modulation which can be obtained by a photodetector. The main drawback is that a high sensitivity may compromise the wavelength operation range [12]. *Passaro et al* [13] reports the spectral scanning as a possible solution, which features a high sensitivity and a large wavelength operation range. On the other hand, most of these interrogators are based on thermal tuning which

limits their interrogation speed to a few kHz. Another approach for interrogation is to use passive interferometers such as Mach-Zehnder interferometers. In combination with a demultiplexing element, such as an AWG, it is possible to interrogate the photonic sensors as demonstrated in [14, 15]. Despite the high sensitivity of this interrogator, special care should be taken to match the spectra of the AWG outputs to the sensors spectra. This might be an issue for integrated sensors such as ring resonators [1] since the resonance wavelength, in most of the cases, cannot be predicted during the design due to variations of the fabrication process.

The interrogation method here proposed may be applied to any sensor whose spectrum is finite and is modulated by an external signal. We demonstrate its performance using FBG sensors, but the method is equally suitable to other types of sensors such as ring resonators. To the best of our knowledge, this is the first interrogator based on integrated Fourier Transform (FT) spectroscopy. The technique is promising since it benefits from high flexibility, high sensitivity, and offers a high tolerance to variations of the fabrication process. In the past, FT spectroscopy was applied to demultiplexing FBG sensors [16, 17], but at that time, the speed of the method was limited by the mechanical speed of the mirror. Integrated photonics enables the design of new FT spectrometer implementations. The most common one consists of an array of MZIs with different optical path lengths (OPDs) [18–22]. Alternatively, [23] uses a single MZI whose OPD can be dynamically increased by using optical switches. The spectrum can be retrieved by calculating the coefficients of the Fourier cosine series from the interferogram [18, 19] or by solving a system of linear equations [20–23]. However, since the number of MZIs is finite, the retrieved spectrum is an approximation to the actual one and a large number of MZIs is required in order to achieve a high spectral resolution.

The design of our integrated FT spectrometer is similar to the one proposed by [24, 25], where the complex Fourier coefficients of the system are obtained by using 3×3 multi-mode interferometers (MMIs). In our case, however, instead of retrieving the spectrum, we demonstrate that the complex Fourier coefficients can be written as a sum of the individual contributions of the sensors. We obtain a coupled system of non-linear equations, whose solution gives the modulation of the sensor's resonance wavelength. Since no approximation has been made, the minimum modulation amplitude we experimentally retrieved is 400 fm, more than two orders of magnitude smaller than the spectral resolution of our own FT spectrometer, and limited only by the signal-to-noise ratio of the input signal. Moreover, we demonstrate that the number of interferometers can be as small as the number of sensors, which strongly reduces the device footprint without compromising the interrogator sensitivity. Finally, we propose a novel technique for compensating the slow drift with time of the phases of the MZIs due to temperature fluctuations [1, 26]. This enables the application of this interrogation method for very low speed photonic sensors. Since the speed is only limited by the electronics, our interrogation method is equally suitable for high speed sensors.

2. Design and characterization of the FT spectrometer

Fig. 1(a) shows a picture of the FT spectrometer. The chip was fabricated in a multi-project wafer run at the Smart Photonics foundry using InP technology. Its dimensions are 4.0 mm by 4.5 mm. The chip has a total of 7 inputs, but inputs #5 and #7 are not used, as indicated in the Fig. 1(a). The cross-section of the waveguide at the facet of the chip is shown in Fig. 1(b) (the mode field diameters are $2.8 \mu\text{m}$ in the horizontal direction and $0.96 \mu\text{m}$ in the vertical direction). This waveguide makes an angle of 7 degrees with respect to a normal line perpendicular to edge of the chip, as shown in Fig. 1(d). The optical fiber guiding the light signal to be coupled to the chip is placed at an angle of 23 degrees with respect to the normal, avoiding that the reflections from the chip facet to be coupled back to the fiber (the angle of 23 degrees can be obtained using Snell's law, giving the fact that the effective index of the waveguide is 3.26 at 1550 nm). The waveguide at input #4 is the only waveguide which makes an angle of 90 degrees with respect to

the chip edge.

By using a taper, the width of the shallow etch waveguide shown in Fig. 1(b) is slowly reduced to $2.0 \mu\text{m}$, where a proprietary component, designed by Smart Photonics, couples the optical field into the deep etch waveguide shown in Fig. 1(c). Compared to the shallow etch waveguide, the deep etch waveguide has a higher mode confinement and it is used everywhere else in the chip. Following the optical path of the main input port (input #1) the light signal is split into nine beams using 1×2 and 2×2 MMIs (the 2×2 MMIs are indicated in the Fig. 1(a); all other power splitters are 1×2 MMIs) and guided to nine different Mach-Zehnder interferometers.

The chip has multiple inputs, each providing access to a specific set of MZIs (see Fig. 1(a)). The main idea is to optimize the optical power budget: in Section 3 it is shown that the number of photonic sensors must be as large as the number of the MZIs. The multiple inputs allow the choice of the number of MZIs to be used during the interrogation. For instance, in order to interrogate up to 5 sensors, it is preferred to use input #6, through which the optical power is shared among MZIs 1-5, instead of input #1. Interrogating the photonic sensors using more MZIs than needed is possible and the extra MZIs may provide some additional information which can be used to increase slightly the signal-to-noise ratio. However, the fringe visibility of the MZIs with larger OPDs are strongly reduced (see the discussion in the end of Section 3.1) and better interrogation results have been obtained by using a small number of MZIs.

One of the key benefits of the FT spectrometers is the large optical throughput (etendue) compared to other types of spectrometers [18, 20, 22]. The design of our FT spectrometer allows the light signal to be coupled from both sides of the chip simultaneously. In this case, it would be needed to split the signal containing the combined spectra of the sensors externally (by using a 1×2 fiber coupler, for instance). This feature has not been explored in this paper, but it could increase the interrogator performance if an additional optical gain is given for the signal to be coupled to the left side of chip, where inputs #2 - #4 provide access to MZIs with larger OPDs (input #1 must not be used, otherwise some of the MZIs would receive the light signal coming from both of chip sides). Thus, the reduced visibility of the MZIs with larger OPDs can be compensated.

MZIs represent the heart of the on-chip FT spectroscopy. The length difference between the arms range from 0.710 mm to 6.39 mm in steps of 0.710 mm . At the end of the MZI, the light signals from the two arms interfere within a 3×3 MMI ($360 \mu\text{m}$ length, $11.4 \mu\text{m}$ width). The chip is glued to a printed circuit board (PCB), to which the chip pads were wire bonded. Outputs per MZI of this PCB were connected to an other PCB which contain three transimpedance amplifiers (TIAs) for the photodetectors and a pre-processing module. This module gives a linear combination of the outputs, as indicated in the schematic shown Fig. 1(e).

In this section we characterize the MZIs of the FT spectrometer by considering its response to one particular wavelength λ . The transmittance for the given wavelength of l -th output of the m -th MZI is given by:

$$T_{ml}(\lambda) = \frac{1}{3} \left[1 + v_{ml} \cos \left(2\pi \frac{n_{eff,m}(\lambda) \Delta L_m}{\lambda} + \phi_l \right) \right], \quad (1)$$

where v_{ml} is the visibility, $n_{eff,m}(\lambda)$ is the effective index of waveguides of the m -th MZI, ΔL_m the arms length difference of the m -th MZI, and ϕ_l is the MZI phase shift given by (120° , 0° , -120°) for $l = 1, 2, 3$ in case the 3×3 coupler is balanced. In our design, the waveguide effective indexes are all the same except by small deviations caused by variations of the fabrication process. Expanding the term $n_{eff,m}(\lambda)/\lambda$ in Taylor series around λ_0 , we obtain:

$$\frac{n_{eff,m}(\lambda)}{\lambda} \cong \frac{n_{eff}(\lambda_0) + n_g + \delta n_{eff,m}}{\lambda_0} - \frac{n_g}{\lambda_0^2} \lambda, \quad (2)$$

where $\delta n_{eff,m}$ are deviations of the nominal value of the effective index at the m -th MZI and λ_0

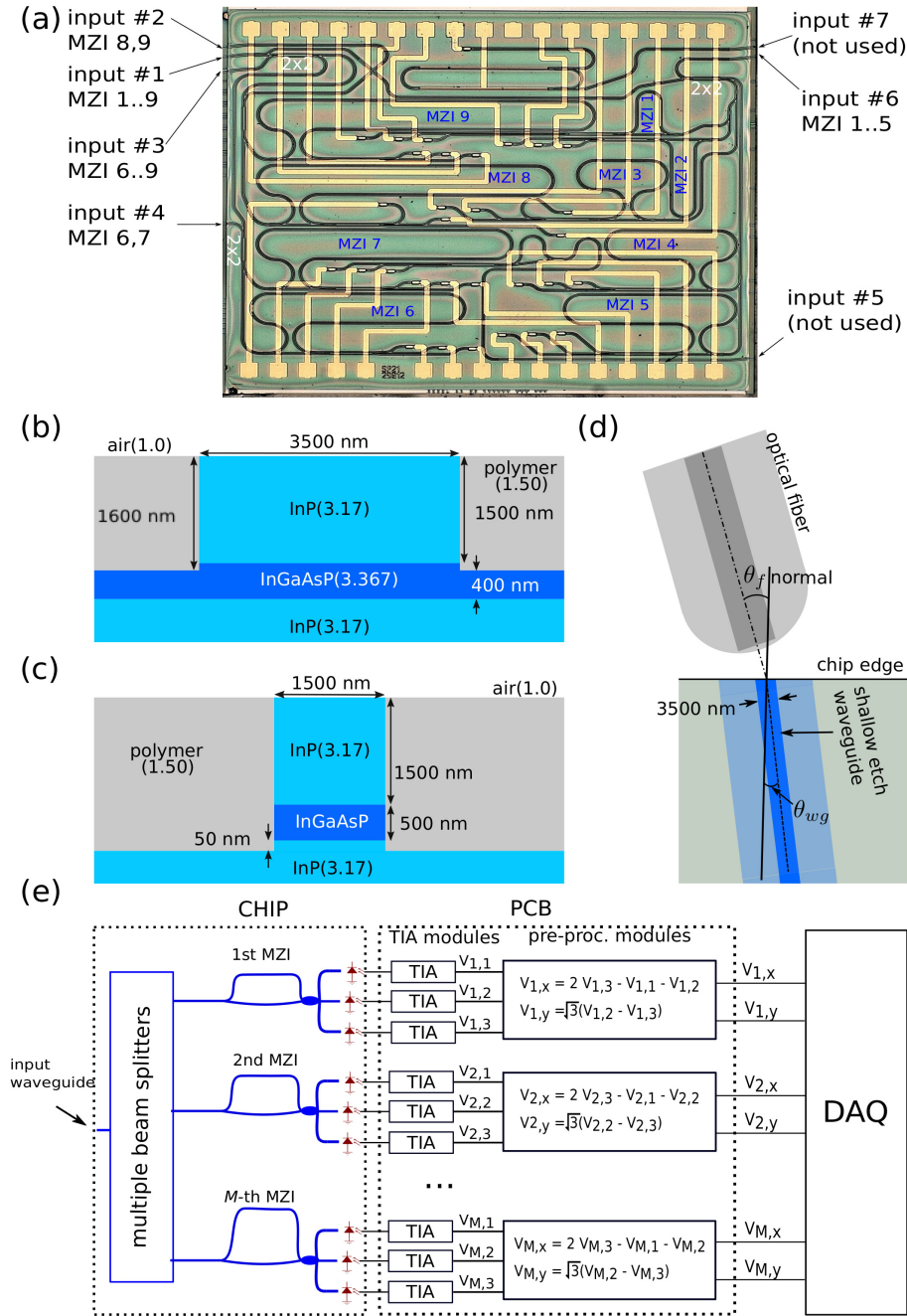


Fig. 1. (a) Picture of the FT spectrometer chip. ΔL_m is given by $\Delta L_m = m\Delta L_1$ with $\Delta L_1 = 0.710$ mm, leading to $F_m = F_1/m$, where m is an integer number ranging from 1 to 9. The different MZIs are identified with the index m . The 2x2 MMIs are indicated in white. All other power splitters are 1x2 MMIs. (b) Cross-section of the shallow etch waveguide. The refractive indexes at the wavelength of 1550 nm are also indicated. (c) Cross-section of the deep etch waveguide. (d) Schematic of an optical fiber aligned to one of the inputs of the chip. For input #4, $\theta_{wg} = \theta_f = 0^\circ$. For all other inputs, $\theta_{wg} = 7^\circ$ and $\theta_f = 23^\circ$. (e) Schematic of the FT spectrometer and the PCB that implements the TIAs and a pre-processing module. The outputs are sampled by the DAQ.

a wavelength close to 1550.0 nm. The approximation holds as long as the effect group index (n_g) can be considered constant over the spectrum of interest. Replacing Eq. (2) in Eq. (1) we obtain:

$$T_{ml}(\lambda) = \frac{1}{3} \left[1 + v_{ml} \cos \left[2\pi \frac{\lambda}{F_m} - \phi_l - \Psi_m \right] \right], \quad (3)$$

where $F_m = \lambda_0^2 / (n_g \Delta L_m)$ is the free spectral range of the m -th interferometer and

$$\Psi_m = \frac{2\pi \Delta L_m}{\lambda_0} (n_g + n_{eff}(\lambda_0) + \delta n_{eff,m}). \quad (4)$$

In our design, ΔL_m is given by $\Delta L_m = m \Delta L_1$ with $\Delta L_1 = 0.710$ mm, leading to $F_m = F_1/m$, where m is an integer ranging from 1 to 9 and $F_1 = 921.7 \pm 0.5$ pm. Ψ_m depends on $n_{eff}(\lambda_0)$, which might change in case of temperature fluctuations, inducing a phase drift in $T_{ml}(\lambda)$.

The schematic of Fig. 1(e) shows that the outputs of the MZIs are connected to integrated photodetectors (PD). The PD current I_{ml} is given by $I_{ml}(\lambda) = P_m R_{ph} T_{ml}(\lambda)$, where P_m is the optical power delivered at the m -th MZI and R_{ph} is the photodetector responsivity. The outputs of the photodetectors are sent to TIAs, whose outputs voltage are given by:

$$V_{ml}(\lambda) = g_{ml} P_m R_{ph} T_{ml}(\lambda) = \frac{g_{ml} P_m R_{ph}}{3} \left[1 + v_{ml} \cos \left(2\pi m \frac{\lambda}{F_1} - \phi_l - \Psi_m \right) \right], \quad (5)$$

where g_{ml} is the transimpedance gain. The 3×3 MMIs were designed to produce interference fringes with similar amplitude and a 120° shift between each other. Aiming for the interrogation of the photonic sensors, the pre-processing module of the PCB combines the TIA output voltages according to [1]:

$$\begin{aligned} V_{m,x}(\lambda) &= 2V_{m,3} - V_{m,1} - V_{m,2} = A_{m,x} \cos \left(2\pi m \frac{\lambda}{F_1} - \Psi_m \right) + x_{off,m}, \\ V_{m,y}(\lambda) &= \sqrt{3} (V_{m,2} - V_{m,3}) = A_{m,y} \sin \left(2\pi m \frac{\lambda}{F_1} - \Psi_m - \delta\phi_m \right) + y_{off,m}, \end{aligned} \quad (6)$$

where $V_{m,x}$ and $V_{m,y}$ are 90° phase shift voltages, $A_{m,x}$ and $A_{m,y}$ are the voltage amplitudes, $x_{off,m}$ and $y_{off,m}$ are voltage offsets, and $\delta\phi_m$ is a phase error. If the 3×3 MMI is balanced and the electronic components of the PCB are ideal (ideal operational amplifiers and no variance with respect to the nominal value of the resistors and capacitors), the voltage offsets are zero ($x_{off,m} = y_{off,m} = 0$), $\delta\phi_m = 0$, and $A_{m,x} = A_{m,y} = P_m R_{ph} g v$, where the visibility is $v = v_{m1} = v_{m2} = v_{m3}$ and the TIA gain is $g = g_{m1} = g_{m2} = g_{m3}$. In this case, the Lissajous curve $[V_{m,x}(\lambda), V_{m,y}(\lambda)]$ gives a circle with radius $v P_m R_{ph} g$ centred at the origin.

The transmission spectrum of each MZI has been measured using a tunable laser (Agilent, 81960A). The laser power is set to 6.0 mW and we performed the laser wavelength sweep ranging from 1550 nm to 1551 nm in steps of 1 pm, while the outputs of the pre-processing module are recorded by the digital acquisition module (DAQ, National Instruments, NI 9220). Fig. 2(a) shows the measured voltages of the outputs of MZI 1 ($\Delta L_1 = 0.710$ mm), as well as a fit of the measured data against to Eq. (6). Since $V_{1,x}$ and $V_{1,y}$ have slightly different amplitudes and $\delta\phi_1 = 17.9^\circ$, the circle is deformed into a tilted ellipse centred outside of the origin, as shown in Fig. 2(b). Non-idealities and variations of electronic components in the PCB are neglected in the following section, whereas the unbalancement of the 3×3 MMI needs to be considered. In Section 3.2 we discuss how to correct for this.

3. Interrogation method and experimental setup

3.1. The interrogation method

Here we derive the expressions for determining the resonance wavelengths of the photonic sensors as a function of time. Typically, the spectrum of each sensor has a peaked lineshape,

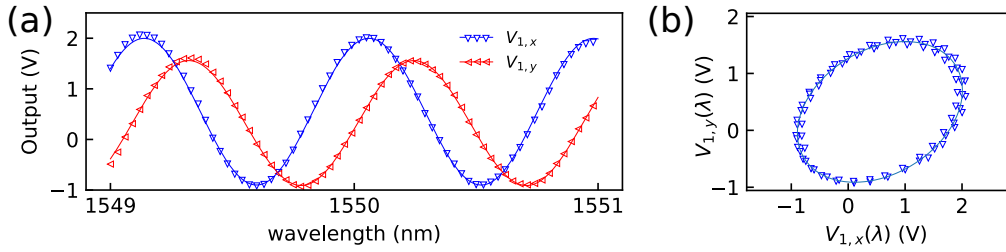


Fig. 2. (a) Traces of $V_{1,x}$ and $V_{1,y}$ as a function of the laser wavelength. We fitted Eq. (6) against the data points and we obtained $F_1 = 921.7 \pm 0.5$ pm, $\delta\phi_1 = 17.9 \pm 0.3^\circ$, $A_{1,x} = 1.449 \pm 0.003$ V and $A_{1,y} = 1.234 \pm 0.004$ V. (b) Lissajous plot of the data points $[V_{1,x}(\lambda), V_{1,y}(\lambda)]$ shown in Fig. 2(a). By fitting an ellipse to the data points we got 1.56 V and 1.09 V for the semi-axis values and 31.2° for the tilt angle with respect to the x -axis.

which is modulated by an external signal such as temperature, strain or any other physical or chemical quantity. The photonic sensors are assumed to be wavelength multiplexed. Let there be K sensors with resonance wavelengths $\lambda_k(t)$ at time t , where $k = 1, \dots, K$. The combined spectrum $S(\lambda, \lambda_1(t), \dots, \lambda_K(t))$ received by the interrogator is given by:

$$S(\lambda, \lambda_1(t), \dots, \lambda_K(t)) = \sum_{k=1}^K s_k(\lambda, \lambda_k(t)) = \sum_{k=1}^K s_k(\lambda - \lambda_k(t)), \quad (7)$$

where $s_k(\lambda, \lambda_k(t))$ is the spectrum of the k -th sensor. The signals that are to be sensed induce time dependent modulations of the resonance wavelengths. The resonances $\lambda_k(t)$ must be separated so that the curves $s_k(\lambda, \lambda_k(t))$ do not overlap. In this paper $s_k(\lambda, \lambda_k(t))$ correspond to the reflection spectra of FBGs sensors. However, the method applies also to integrated photonic sensors as the ones described in [1].

$S(\lambda)$ is assumed to be a poly-chromatic signal and the values of the TIA output voltages are given by:

$$V_{ml}(t) = G \int_{-\infty}^{\infty} S(\lambda, \lambda_1(t), \dots, \lambda_K(t)) T_{ml}(\lambda) d\lambda, \quad (8)$$

where the constant G is given by $G = (1 - \alpha_c)gR_{ph}$ with α_c the coupling losses. The electronic pre-processing module combines the signals from the three outputs of the interferometers according to Eq. (6), resulting in the two 90° phase shifted voltages $V_{m,x}(t)$ and $V_{m,y}(t)$:

$$V_{m,x}(t) = 3G \int_{-\infty}^{\infty} S(\lambda, \lambda_1(t), \dots, \lambda_K(t)) \cos\left(2\pi m \frac{\lambda}{F_1} - \Psi_m\right) d\lambda + x_{off,m}, \quad (9)$$

$$V_{m,y}(t) = 3G \int_{-\infty}^{\infty} S(\lambda, \lambda_1(t), \dots, \lambda_K(t)) \sin\left(2\pi m \frac{\lambda}{F_1} - \Psi_m\right) d\lambda + y_{off,m}. \quad (10)$$

As explained in Section 2, the voltage offsets $x_{off,m}$ and $y_{off,m}$ are mainly caused by the fact that the 3×3 MMIs are unbalanced. At the end of a calibration process (see Section 3.2), the offsets are removed by averaging and, at this point, they are neglected.

By defining a complex voltage $\hat{V}_m(t) = V_{m,x}(t) + iV_{m,y}(t)$ we obtain:

$$\hat{V}_m(t) = 3Ge^{-i\Psi_m} \int_{-\infty}^{\infty} S(\lambda, \lambda_1(t), \dots, \lambda_K(t)) \exp\left(i2\pi \frac{m}{F_1} \lambda\right) d\lambda. \quad (11)$$

The chip is characterized after the MZI phase drift has been stabilized, so Ψ_m is constant in time and taken out of the integral in Eq. (11). In Section 3.3, however, a novel method is presented

for compensating the environmental phase drift by using one of the sensors as a reference. We assume that $S(\lambda, \lambda_1(t), \dots, \lambda_K(t))$ vanishes outside the interval $[\lambda_0 - F_1/2, \lambda_0 + F_1/2]$ for all times t , where λ_0 is a wavelength close to 1550.0 nm. Then we have:

$$\frac{\hat{V}_m(t)e^{i\Psi_m}}{3G} = \int_{\lambda_0 - F_1/2}^{\lambda_0 + F_1/2} S(\lambda, \lambda_1(t), \dots, \lambda_K(t)) \exp\left(i2\pi \frac{m}{F_1} \lambda\right) d\lambda. \quad (12)$$

Eq. (12) are the Fourier coefficients of the function $\lambda \rightarrow S(\lambda, \lambda_1(t), \dots, \lambda_K(t))$ when considered as periodic function with period F_1 . This implies that:

$$\begin{aligned} S(\lambda, \lambda_1(t), \dots, \lambda_K(t)) &= \frac{1}{3G} \sum_{m=-\infty}^{\infty} \hat{V}_m(t)e^{i\Psi_m} \exp\left(-i2\pi \frac{m}{F_1} \lambda\right) \\ &= \frac{2}{3G} \sum_{m=0}^{\infty} \left[V_{m,x}(t) \cos\left(2\pi \frac{m}{F_1} \lambda - \Psi_m\right) - V_{m,y}(t) \sin\left(2\pi \frac{m}{F_1} \lambda - \Psi_m\right) \right], \end{aligned} \quad (13)$$

where $\hat{V}_{-m}(t) = \hat{V}_m^*(t)$ since $S(\lambda, \lambda_1(t), \dots, \lambda_K(t))$ is real. The chip contains a finite number of $M = 9$ interferometers. The retrieved spectrum $S_M(\lambda, \lambda_1(t), \dots, \lambda_K(t))$ is given by:

$$S_M(\lambda, \lambda_1(t), \dots, \lambda_K(t)) = \frac{2}{3G} \sum_{m=0}^M \left[V_{m,x}(t) \cos\left(2\pi \frac{m}{F_1} \lambda - \Psi_m\right) - V_{m,y}(t) \sin\left(2\pi \frac{m}{F_1} \lambda - \Psi_m\right) \right]. \quad (14)$$

Function $S(\lambda, \lambda_1(t), \dots, \lambda_K(t))$ differs from $S_M(\lambda, \lambda_1(t), \dots, \lambda_K(t))$ by the fact that the last one features a finite spectral resolution $\delta\lambda_{res}$ given by:

$$\delta\lambda_{res} = \frac{F_1}{2M}. \quad (15)$$

For $M = 9$, $\delta\lambda_{res} = 50$ pm. Moreover, $S_M(\lambda, \lambda_1(t), \dots, \lambda_K(t))$ is periodic with period F_1 . For a large number of interferometers ($M \gg K$), $S_M(\lambda, \lambda_1(t), \dots, \lambda_K(t))$ gives a good approximation to $S(\lambda, \lambda_1(t), \dots, \lambda_K(t))$ and it is possible to obtain the resonance wavelengths by tracking the peaks of $S_M(\lambda, \lambda_1(t), \dots, \lambda_K(t))$. However, $\delta\lambda_{res}$ represents a limitation to the minimum modulation amplitude to be experimentally obtained.

In order to determine $\lambda_k(t)$ with higher accuracy and using a reduced number of MZIs we derive a non-linear system of equations. We assume in this section that $\lambda(t)$ is known at $t = 0$. Let

$$\lambda_k(t) = \lambda_k(0) + \delta_k(t), \quad (16)$$

where $\delta_k(t)$ is the modulation of the resonance wavelength of the k -th sensor that we aim to determine. By substituting Eq. (7) and Eq. (16) into Eq. (11), we obtain:

$$\hat{V}_m(t) = 3Ge^{-i\Psi_m} \sum_{k=1}^K \int_{-\infty}^{\infty} s_k(\lambda - \lambda_k(0) - \delta_k(t)) \exp\left(i2\pi \frac{m}{F_1} \lambda\right) d\lambda. \quad (17)$$

The right-hand side of Eq. (17) represents the Fourier transform of $s_k(\lambda - \lambda_k(0) - \delta_k(t))$ evaluated at m/F_1 . Using the shift property of the Fourier transformation, Eq. (17) is rewritten as:

$$\hat{V}_m(t) = 3G \sum_{k=1}^K \hat{s}_k(m/F_1) \exp\left[i\left(-\Psi_m + 2\pi \frac{m}{F_1} \lambda_k(0)\right)\right] \exp\left(i2\pi \frac{m}{F_1} \delta_k(t)\right), \quad (18)$$

where $\hat{s}_k(m/F_1)$ is the Fourier transform of $s_k(\lambda)$. Let

$$a_{mk} = 3G \hat{s}_k(m/F_1) \exp\left[i\left(-\Psi_m + 2\pi \frac{m}{F_1} \lambda_k(0)\right)\right]. \quad (19)$$

We rewrite Eq. (18) as:

$$\hat{V}_m(t) = \sum_{k=1}^K a_{mk} \exp \left[\left(i \frac{2\pi}{F_1} \delta_k(t) \right)^m \right], \quad (20)$$

for $m = 1, \dots, M$. The coefficients a_{mk} are experimentally determined as explained in Section 3.2. Eq. (20) represents an $M \times K$ system of non-linear equations to be solved using Newton's method, where M is the number of interferometers and K is the number of sensors. Hence, the number of interferometers must only be at least as large as the number of sensors (i.e. $M \geq K$), which means that the footprint of the device can be relatively small. In our chip $M = 9$. The system is explicitly written in the in Eq. (21):

$$\begin{aligned} \hat{V}_1(t) &= a_{11} \exp \left[i \frac{2\pi\delta_1(t)}{F_1} \right] + a_{12} \exp \left[i \frac{2\pi\delta_2(t)}{F_1} \right] + \dots + a_{1K} \exp \left[i \frac{2\pi\delta_K(t)}{F_1} \right], \\ \hat{V}_2(t) &= a_{21} \exp \left[2i \frac{2\pi\delta_1(t)}{F_1} \right] + a_{22} \exp \left[2i \frac{2\pi\delta_2(t)}{F_1} \right] + \dots + a_{2K} \exp \left[2i \frac{2\pi\delta_K(t)}{F_1} \right], \\ &\dots \\ \hat{V}_M(t) &= a_{M1} \exp \left[Mi \frac{2\pi\delta_1(t)}{F_1} \right] + a_{M2} \exp \left[Mi \frac{2\pi\delta_2(t)}{F_1} \right] + \dots + a_{MK} \exp \left[Mi \frac{2\pi\delta_K(t)}{F_1} \right]. \end{aligned} \quad (21)$$

It can be show that as long as the phases $2\pi\lambda_k(t)/F_1$ (for $k = 1, \dots, K$) are different and the initial guess for $\{\delta_1(t), \dots, \delta_K(t)\}$ is close to the actual solution, the Jacobian $\partial\hat{V}_m/\partial\delta_k$ is not singular and the Eqs. (21) are independent. From Eq. (16), at $t = 0$, $\{\delta_1(0), \dots, \delta_K(0)\} = \{0, \dots, 0\}$. The solution at time t is taken as an initial guess at $t + 1/f_s$, where f_s is the sampling frequency. This reduces the computational time and assures that the initial guess and the solution are close to each other. The method is also flexible in the sense that the ratio between the arms length difference of the MZIs ($\Delta L_m/\Delta L_1$) does not need to be an integer number, which would cause the m value in Eq. (20) to a fractional number. The equations remain independent as long as the ΔL_m values are different.

Assuming that the FBG sensors spectra have a Lorentzian lineshape, we replace the Fourier transform of $s_k(\lambda)$ into Eq. (19):

$$a_{mk} = \frac{3Gs_k^{\max}}{2} \exp \left(\frac{-mOPD_1}{L_{c,k}} \right) \exp \left[i \left(-\Psi_m + 2\pi \frac{m}{F_1} \lambda_k(0) \right) \right], \quad (22)$$

where s_k^{\max} is the maximum value of the Lorentzian of the k -th sensor, $OPD_1 = n_g \Delta L_1$ is the optical path difference of MZI 1, and $L_{c,k}$ is the cohenrece length given by:

$$L_{c,k} = \frac{\lambda_0^2}{\pi w_k}, \quad (23)$$

where w_k is the full width half maxima (FWHM) of the Lorentzian. The coherence length limits the maximum OPD value which allows interferometric fringes to be experimentally resolved. Eq. (22) shows that a_{mk} becomes very small when the MZI free spectral range is comparable or smaller than the FWHM of k -th sensor. As discussed in Section 4, the MZIs with larger OPDs are not used due to the strong attenuation and the reduced signal-to-noise ratio (SNR).

3.2. Calibration and experimental determination of the coefficients

The coefficients a_{mk} are experimentally determined via the following calibration procedure. Let t_k^{start} be the instant of time when the calibration of k -th sensor starts and t_k^{end} be the instant of time when the calibration ends for the same sensor. During the time interval $t_k^{\text{start}} < t < t_k^{\text{end}}$, all sensors are kept at rest, while sensor k is excited. In case sensor k is a temperature sensor,

heat is applied (as much as possible) during the calibration. If sensor k is a strain sensor, a large stress is applied (as much as possible). According to Eq. (20), for a balanced 3×3 MMI, the m -th complex voltage $\hat{V}_m(t)$ during the time interval $t_k^{start} < t < t_k^{end}$ is given by:

$$\hat{V}_m(t) = a_{mk} e^{i2\pi \frac{m}{F_1} \delta_k(t)} + \sum_{l \neq k}^K a_{ml} = |a_{mk}| e^{i\theta_{mk}(t)} + c_{mk}, \quad (24)$$

where $\delta_l(t) = 0$ if $l \neq k$ since no excitation is applied to the other sensors and where $c_{mk} = \sum_{l \neq k}^K a_{ml}$ and $\theta_{mk}(t)$ is the complex argument of the term $a_{mk} e^{im2\pi\delta_k(t)/F_1}$, given by:

$$\theta_{mk}(t) = m2\pi \frac{\delta_k(t)}{F_1} + \arg(a_{mk}). \quad (25)$$

The Lissajous curve $(\Re\{\hat{V}_m(t)\}, \Im\{\hat{V}_m(t)\})$ for $t_k^{start} < t < t_k^{end}$ is given by a circular arc:

$$\begin{aligned} (V_{m,x}(t), V_{m,y}(t)) \Big|_{t_k^{start} < t < t_k^{end}} &= (\Re\{\hat{V}_m(t)\}, \Im\{\hat{V}_m(t)\}) \Big|_{t_k^{start} < t < t_k^{end}} \\ &= [|a_{mk}| \cos(\theta_{mk}(t)) + \Re\{c_{mk}\}, |a_{mk}| \sin(\theta_{mk}(t)) + \Im\{c_{mk}\}] \Big|_{t_k^{start} < t < t_k^{end}}, \end{aligned} \quad (26)$$

where $(\Re\{c_{mk}\}, \Im\{c_{mk}\})$ defines the arc centre, $|a_{mk}|$ the radius, and $\theta_{mk}(t)$ the instantaneous angle with the real axis.

Fig. 3 shows a simulation of the calibration for two sensors. The calibration starts at $t = t_0 < 0$ and ends at $t = 0$, when the interrogation procedure starts. During $t_1^{start} < t < t_1^{end}$, sensor 2 is kept at rest, while sensor 1 is excited by moving its resonance wavelength from 1550.50 nm to 1550.16 nm, as shown in Fig. 3(a). This induces the oscillations of $V_{1,x}(t)$ and $V_{1,y}(t)$ during $t_1^{start} < t < t_1^{end}$ as shown in Fig. 3(b), which are traced as a circular arc in red shown in Fig. 3(c). The procedure is repeated for sensor 2: during $t_2^{start} < t < t_2^{end}$, while sensor 1 is not excited, sensor 2 changes its resonance from 1550.75 nm to 1550.33 nm. This causes the oscillations from $t_2^{start} < t < t_2^{end}$ in Fig. 3(b) which are traced as the circular arc in green shown in Fig. 3(c).

As explained in [1], a slight non-ideal behavior of amplitude and phase of 3×3 couplers are not uncommon and result into a deformation of the circle in an ellipse. An ellipse is fitted to the data points $(V_{m,x}(t)', V_{m,y}(t)')$ during the interval $t_k^{start} < t < t_k^{end}$, where $V_{m,x}(t)'$ and $V_{m,y}(t)'$ are the m -th MZI voltages measured during the calibration. A larger excitation of the k -th sensor results in a larger angular deflection, leading to a more accurate retrieval of geometrical parameters of the ellipse. The fitting gives the ellipse semi-axis $r_{1,mk}$ and $r_{2,mk}$ (where $r_{1,mk} > r_{2,mk}$), the angle α that represents the rotation of the ellipse with respect to the x-axis, and the ellipse centre $(x_{mk}^{el}, y_{mk}^{el})$. In order to map the ellipse to a circle, the following transformation is applied:

$$\begin{pmatrix} V_{m,x}(t) \\ V_{m,y}(t) \end{pmatrix} = \begin{pmatrix} r_{1,mk}/r_{2,mk} & 0 \\ 0 & 1 \end{pmatrix} \begin{pmatrix} \cos \alpha & \sin \alpha \\ -\sin \alpha & \cos \alpha \end{pmatrix} \begin{pmatrix} V_{m,x}(t)' \\ V_{m,y}(t)' \end{pmatrix}, \quad (27)$$

where $V_{m,x}$ and $V_{m,y}$ are the corrected values of the 90° phase shifted voltages so that the Lissajous curve $(V_{m,x}(t), V_{m,y}(t))$ for $t_k^{start} < t < t_k^{end}$ gives a circle arc with radius $r_{1,mk}$. The correction of Eq. (27) needs to be performed for all interferometers ($m = 1, \dots, M$). Although the ellipse semi-axis $r_{1,mk}$ and $r_{2,mk}$, as well as the corrected radius $r_{1,mk}$ may change according to the sensor (since it depends on its total transmitted or reflected power spectrum) and according to the interferometer (due to the different MZI's coherence lengths), the ellipse eccentricity depends only on the 3×3 MMI, as discussed in Section 2. Thus, for a given interferometer m the ratio $r_{1,mk}/r_{2,mk}$ is constant for $k = 1, \dots, K$. The design of the 3×3 MMI is the same for all

interferometers, hence the ratio $r_{1,m}/r_{2,m}$ is constant for $m = 1, \dots, M$ as long as the variations of the fabrication process are negligible.

After calculating the 90° phase shifted voltages, the modulus of the coefficients a_{mk} can be obtained. Since the radius of the circle arc obtained for the m -th interferometer and the k -th sensor is $r_{1,mk}$, the modulus of the coefficients a_{mk} , according to Eq. (26), is given by:

$$|a_{mk}| = r_{1,mk}. \quad (28)$$

Next, the linear transformation of Eq. (27) is applied to the point $(x_{mk}^{el}, y_{mk}^{el})$, which gives the centre $(\Re\{c_{m,k}\}, \Im\{c_{m,k}\})$. The angles $\theta_{mk}(t)$ (for $m = 1, \dots, M$ and $k = 1, \dots, K$) are given by:

$$\theta_{mk}(t) = \arctan_2(V_{y,m}(t) - \Im\{c_{m,k}\}, V_{x,m}(t) - \Re\{c_{m,k}\}), \quad (29)$$

where $\arctan_2(x, y)$ is the four quadrant arc tangent. During the final stage of the calibration of sensor k , the angle $\theta_{mk}(t)$ remains constant because then no excitation is anymore applied to it. By substituting $t = t_k^{end}$ in Eq. (25), we obtain:

$$\theta_{mk}(t_k^{end}) = m2\pi \frac{\delta_k(t_k^{end})}{F_1} + \arg(a_{mk}) = m2\pi \frac{\delta_k(0)}{F_1} + \arg(a_{mk}), \quad (30)$$

where the calibration procedure ends at $t = 0$. According to Eq. (16), $\delta_k(0) = 0$. Therefore, the argument of a_{mk} is given by:

$$\arg(a_{mk}) = \theta_{mk}(t_k^{end}) = \theta_{mk}(0). \quad (31)$$

The values of $\lambda_k(t)$ (for $k = 1, \dots, K$) are in general unknown at the end of the calibration ($t = 0$), which contradicts the assumption made in Eq. (16). Here, we refine our previous statement by assuming that the values of $\lambda_k(t)$ are known at $t = t_0$, before the calibration procedure starts. In most of cases, however, the sensors can be calibrated in such a way that their resonance wavelengths return to their initial value at the end of the calibration ($\lambda_k(t_0) = \lambda_k(0)$). In situations where this is not possible (due to a sensor hysteresis, for instance), the values of $\lambda_k(0)$ can be obtained by following the procedure: (a) determine the value of $\delta(t_k^{start})$ from Eq. (25) evaluated at $t = t_k^{start}$; (b) substitute the value of $\delta(t_k^{start})$ in Eq. (16) (also evaluated at $t = t_k^{start}$).

After finishing the calibration of all sensors in this way, the offsets are determined by averaging:

$$\begin{aligned} x_{off,m} &= \frac{1}{|t_0|} \int_{t_0}^0 \left\{ V_{m,y}(t) - \sum_k |a_{mk}| \cos[\theta_{mk}(t)] \right\} dt, \\ y_{off,m} &= \frac{1}{|t_0|} \int_{t_0}^0 \left\{ V_{m,y}(t) - \sum_k |a_{mk}| \sin[\theta_{mk}(t)] \right\} dt. \end{aligned} \quad (32)$$

Finally, the complex voltages are computed as function of time to be used in Eqs. (20) and (21):

$$\hat{V}_m(t) = [V_{x,m}(t) - x_{off,m}] + i [V_{y,m}(t) - y_{off,m}]. \quad (33)$$

3.3. Compensation of the phase drift

Since the effective index in Eq. (4) is temperature dependent, local variations of temperature induces the phase Ψ_m to drift. [22] presents two different methods for compensating the phase drift: by using temperature dependent calibration matrices or by correcting the phases errors of the interferogram in case of narrowband signals. In our case, however, the system of equations is non-linear and a different approach is used. Eq. (4) is rewritten according to:

$$\Psi_m(t) = m \frac{2\pi\Delta L}{\lambda_0} \left(n_g + n_{eff}(\lambda_0)(T_0) + \frac{\partial n_{eff}}{\partial T} \Delta T(t) + \delta n_{eff,m} \right) = \Psi_m(0) + m\Delta\Psi(t), \quad (34)$$

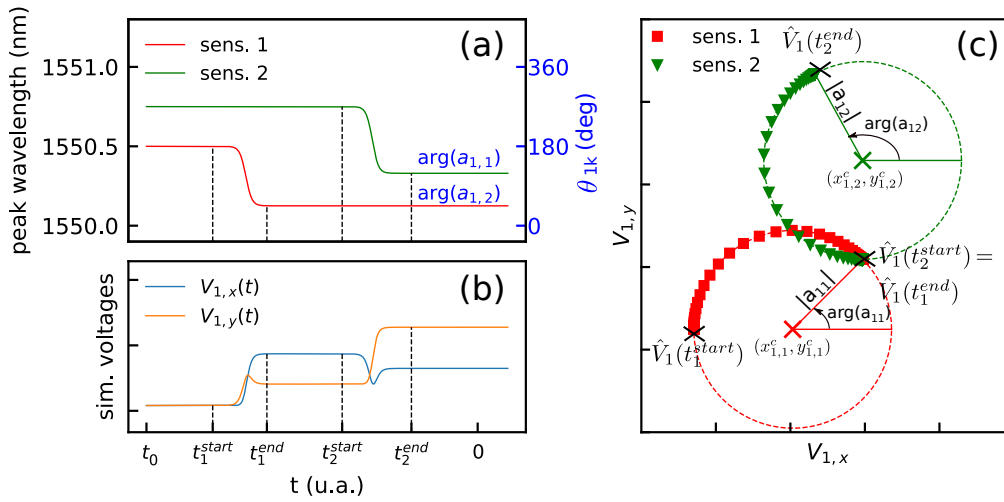


Fig. 3. Illustration of the calibration procedure for two sensors. (a) Independent excitation of sensor 1 and sensor 2. (b) Simulated values of $V_{1,x}(t)$ and $V_{1,y}(t)$ for MZI 1. The changes in time of the functions $V_{1,x}(t)$ and $V_{1,y}(t)$ are caused by the modulation of the peak wavelengths shown in Fig. 3(a). The voltages $V_{m,x}(t)'$ and $V_{m,y}(t)'$ ($m = 1, \dots, M$) are measured by our acquisition system. $V_{m,x}(t)$ and $V_{m,y}(t)$ are obtained from Eq. (27). For this simulation, $V_{m,x}(t) = V_{m,x}(t)'$ and $V_{m,y}(t) = V_{m,y}(t)'$. (c) Lissajous curve ($V_{1,x}(t)$, $V_{1,y}(t)$) for MZI 1. The modulation of the peak wavelength of the sensors induces an angular deflection in the plane of the voltages $V_{1,x}$ and $V_{1,y}$. From the Lissajous curve, the complex modulus and the phase of the coefficients a_{mk} were extracted. For this simulation, $F_1 = 1.0$ nm.

where

$$\Delta\Psi(t) = \frac{2\pi\Delta L}{\lambda_0} \frac{\partial n_{eff}}{\partial T} \Delta T(t). \quad (35)$$

The temperature dependence of the group index n_g and to δn_{eff} have been neglected. Eq. (35) indicates that the phases Ψ_m in Eq. (18), (20), and (21) are no longer constant. Eq. (18) can be rewritten as:

$$\begin{aligned} \hat{V}_m(t) &= 3G \sum_{k=1}^K \hat{s}_k(m/F_1) \exp \left[i \left(-\Psi_m(0) + 2\pi \frac{\lambda_k(0)}{F_1} \right) \right] \exp \left[i 2\pi \frac{m}{F_1} \left(\delta_k(t) - \Delta\Psi(t) \frac{F_1}{2\pi} \right) \right] \\ &= \sum_{m=1}^M a'_{mk} \exp \left[\left(i 2\pi \frac{m}{F_1} \delta_k(t)' \right)^m \right], \end{aligned} \quad (36)$$

where

$$\delta_k(t)' = \delta_k(t) - \Delta\Psi(t)F_1/(2\pi). \quad (37)$$

The right side of Eq. (36) is identical to Eq. (20) demonstrating that fluctuations of the environmental phase impacts on the solutions of Eq. (20) or Eq. (36). This effect can be corrected by using another sensor as a reference, to which no excitation is applied and its temperature is kept constant.

Let $\delta_{ref}(t)$ be the solution of Eq. (36) for the reference sensor. The calibration procedure assures that when the interrogation procedure starts ($t = 0$), the values $\delta_k(0)$ are zero for all sensors ($k = 1, \dots, K$). Since no excitation is applied to the reference sensor, the function $\delta_{ref}(t)$ remains at zero for $t > 0$. Hence, according to Eq. (37):

$$\delta_{ref}(t)' = -\Delta\Psi(t)F_1/(2\pi). \quad (38)$$

Thus, the phase drift can be compensated by subtracting the term $\Delta\Psi(t)F_1/(2\pi)$ in Eq. (37), obtained from Eq. (38):

$$\delta_k(t) = \delta_k(t)' - \delta_{ref}(t)' \quad (39)$$

3.4. Experimental setup

The schematics of the experiment is depicted in Fig. 4. Light from a broadband amplified spontaneous emission source (ASE, Optolink, OLS15CGB-20-FA) is sent, through a circulator (OZ Optics, FOC-12N-111-9), to the FBG sensor array (Technicasa, T10). The broadband source has an approximately flat spectrum, ranging from 1525 nm to 1565 nm. The FBG sensors reflect back to the circulator their combined spectrum, which is amplified by an optical booster amplifier (Thorlabs, S9FC1004P) according to Fig. 4(a). The gain is 12 dB and the light is coupled to the chip using lensed fibers (Oz Optics, TSMJ-3A-1550-9). The lensed fiber is placed at an angle of 23° with respect a normal line perpendicular to the edge of the chip (see Fig. 1(d)). Outputs of the chip are conveyed to a PCB which implements the transimpedance amplifiers for the photodetectors and a pre-processing module in order to implement Eq. (6) electronically (see Fig. 1(e)). The PCB outputs are sampled by the DAQ (National instruments, NI9220), which the maximum sampling speed is 100 kSa/s/channel.

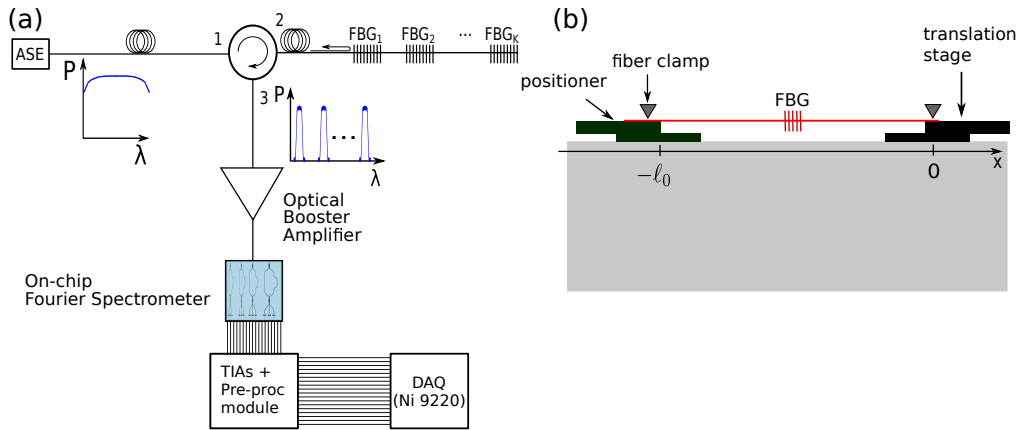


Fig. 4. (a) Schematic of the setup. Light from an ASE source is sent, through a circulator, to the FBG sensor array. The FBG sensors reflect back to the circulator their combined spectrum, which is amplified by an optical booster amplifier (gain = 12dB). Light is coupled to the chip using lensed fibers. (b) Schematic of the temperature / strain sensors. $\ell_0 = 1.74$ m, which is the fiber length between the clamps.

The performance of our interrogator is evaluated using four FBG sensors: three as strain sensors one as a reference sensor, used to compensate the environmental phase drift. The reflection spectrum of the FBGs have a peak lineshape. The FWHM is 103 pm and their resonance wavelengths without applied stress is 1550.0 ± 0.5 nm. The calibration is performed in a such way that $\lambda_k(t_0) = \lambda_k(0)$. The ends of the fibers containing the FBGs are clamped to the translation stages as shown in Fig. 4(b). In order to tune the resonance wavelengths $\lambda_k(0)$, stress is applied using the manual positioners, avoiding the angles $2\pi(\lambda_k(t))/F_1$ to overlap during the experiment. FBG #1 represents the main strain sensor and the translation stage (referred as translation stage 1) to which FBG #1 is attached is controlled by a stepper motor. FBGs #2 and #3 are the secondary strain sensors and they are both attached to translation stage 2 controlled by another stepper motor. FBG #4 is the reference sensor and it is attached only to manual positioners. We programmed the stepper motors to operate in cycles of three steps: (a) the translation stage travels at a constant

speed from the position $x = 0$ to $x = \Delta\ell$; (b) The stage rests at $x = \Delta\ell$; (c) The stage returns to the original position.

Since FBGs #2 and #3 are secondary strain sensors, we programmed the translation stage to move periodically from the distances $x = 0$ to $x = \Delta\ell^{(2)} = 30\mu\text{m}$. In contrast, the translation stage to which FBG #1 is attached, travels to different values of $\Delta\ell^{(1)}$ ranging from $0.5\mu\text{m}$ to $200\mu\text{m}$ (these values are shown later in Fig. 6). Since the stress to be applied to FBG #1 is much larger compared to FBGs #2 and #3, the translation stage 1 is programmed to move towards $-x$. Thus, a negative stress applied to FBG #1, avoiding to damage it. Translation stage 1 repeats three times its motion from $x = 0$ to $x = \Delta\ell^{(1)}$ and from $x = \Delta\ell^{(1)}$ to $x = 0$. Thus, the travelling distances $\Delta\ell_{3j+1}^{(1)}$, $\Delta\ell_{3j+2}^{(1)}$ and $\Delta\ell_{3j+3}^{(1)}$ are the same for $j = 0, \dots, J-1$, where J is the number of different values of $\Delta\ell^{(1)}$.

4. Experimental results

As explained in Section 3.4, the performance of our interrogator is evaluated using four FBG sensors: three as strain sensors one as a reference sensor, used to compensate the environmental phase drift. Using manual positioners, a constant stress is applied to all FBGs in such a way that the resonance wavelengths of the sensors are set to $\lambda_1(0) = 1550.9\text{ nm}$, $\lambda_2(0) = 1550.3\text{ nm}$, $\lambda_3(0) = 1551.4\text{ nm}$ and $\lambda_4(0) = 1549.7\text{ nm}$. The differences of $\lambda_k(t) - \lambda_l(t)$ for $l \neq k$ can be larger than F_1 (F_1 is the free spectral range of MZI 1) provided that the angles $2\pi\lambda_k(t)/F_1 \neq 2\pi\lambda_l(t)/F_1$ for all $l, k = 1 \dots K$. The light signal is coupled to the chip using input #6 (see Fig. 1(a)), where the input power is shared among MZIs 1 to 5. Better interrogation results are obtained by sharing the optical power among a reduced number of interferometers since the outputs of the MZIs with larger OPDs are strongly attenuated, according to the discussion in the end of Section 3.1.

In order to retrieve the coefficients a_{mk} , we individually excited the FBG sensors. Following the procedure described in Section 3.2, the complex voltages $\hat{V}_m(t)$ have been obtained by mapping the ellipse arcs to circle arcs according to Eq. (27), and by removing the voltage offsets according to Eq. (32). Fig. 5(a) shows the real and imaginary parts of $\hat{V}_1(t)$, to which a low pass filter (cut-off at 45 Hz) has been applied in order to suppress noise. The real and the imaginary parts of $\hat{V}_1(t)$, shown in Fig. 5(a), are plotted in Fig. 5(b) as a Lissajous curve. Fig. 5(b) shows four circular arcs, which correspond to the individual excitation of the sensors, obtained from the outputs of MZI $m = 1$ during the calibration. The radii and the angles of the arcs at the end of the calibration procedure give the modulus and argument of the coefficients a_{mk} , as described in Section 3.2.

Fig. 5(b) shows, however, that some regions of the Lissajous curve deviate from the expected circular path. This occurs when the resonance wavelengths of two FBGs are about to cross and the spectra of two FBG sensors overlap. This causes that a part of the input optical signal is reflected multiple times in between the FBGs, creating an Fabry-Perot cavity. The interference of the electric field which is reflected multiple times between the FBGs leads to the deviations of the circular arcs. To overcome this issue, we followed the calibration described in Section 3.2 using only the parts of the Lissajous curves that are close to circular. For $t > 0$ s, the interrogation starts and the three strain sensors are simultaneously excited. As a result, an arbitrary Lissajous curve is obtained.

Figs. 5(c)-5(f) show the solution of Eq. (20) obtained using the Newton's method. As explained in Section 3.1, the solution obtained at the instant t is used as an initial guess for the Newton's method at the instant $t + 1/f_s$, where f_s is the sampling frequency. As a result, the method converges at any t with a maximum of four interactions. For a sampling rate of 10 kSa/s, about one million of systems of equations needs be solved from $t = 0$ s to $t = 100$ s. Using an Intel i5-3470 processor, the solution is roughly calculated at a rate of a hundred equations per second and the total computational time is about 2h and 45 min.

FBGs #2 and #3 are attached to translation stage 2 which periodically travels from $x = 0$ to

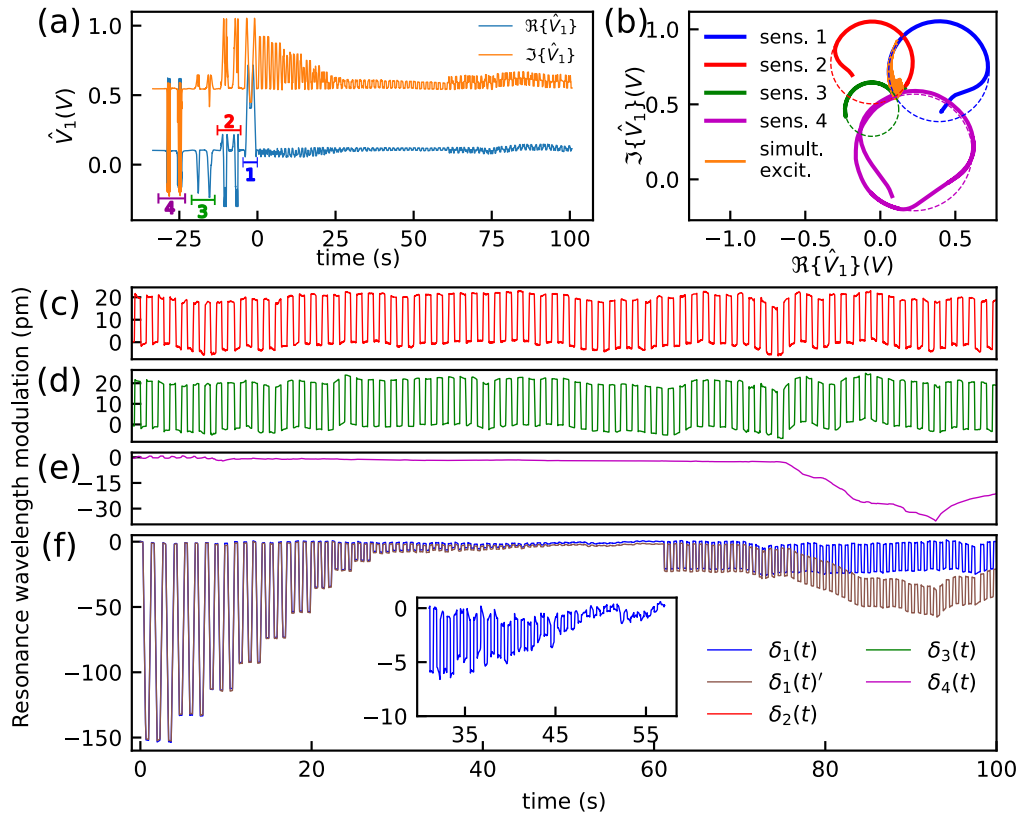


Fig. 5. Main results of the interrogation. (a) Time traces of the real and imaginary parts of $\hat{V}_1(t)$. A low pass filter (cut-off at 45 Hz) has been applied to the measured voltages $V_{m,x}(t)$ and $V_{m,y}(t)$. The numbers 1,2,3 and 4 indicate the calibration interval ($t_k^{start} < t < t_k^{end}$) for sensors $k = 1, \dots, 4$. (b) Lissajous plot obtained by plotting the real and imaginary parts of $\hat{V}_1(t)$. During the calibration, the Lissajous curve is a circular arc. During the interrogation, all sensors are simultaneously excited, and an arbitrary Lissajous curve is obtained as shown in orange. (c)-(e) Solutions $\delta_2(t)$, $\delta_3(t)$ and $\delta_4(t)'$ of Eq. (36) for $t > 0$. FBG #4 is the reference sensor. The phase drift was compensated using Eq. (39). (f) Comparison between the solutions $\delta_1(t)$ and $\delta_1(t)'$. The inset shows a zoom of the solution $\delta_1(t)$.

$x = \Delta\ell^{(2)} = 30\mu\text{m}$. As a result, the functions $\delta_2(t)$ and $\delta_3(t)$ are time periodic, as shown in Figs. 5(c) and 5(d). On the other hand, Fig. 5(f) shows the solution $\delta_1(t)$, which consists of a succession of dips. The dips are obtained because the stepper motor applies a negative stress to FBG #1, as explained in Section 3.4. Since the translation stage repeats its motion three times to a given distance $\Delta\ell^{(1)}$, Fig. 5(f) shows a series of dips grouped by 3 successive ones with approximately the same depth.

Fig. 6 shows the modulation amplitude $\Delta\lambda^{(1)}$ for sensor 1 as a function of the strain applied to FBG #1. The strain is assumed to be constant along the fiber and it is defined as:

$$\varepsilon_j^{(1)} = \frac{\Delta\ell_{3j}^{(1)}}{\ell_0}, \quad (40)$$

where $\varepsilon_j^{(1)}$ is the strain at FBG #1 and ℓ_0 the fiber length defined in Fig. 4(b). The index $3j$ in Eq. (40) appears since the distances $\Delta\ell_{3j}^{(1)}$, $\Delta\ell_{3j+1}^{(1)}$ and $\Delta\ell_{3j+2}^{(1)}$ are the same, as explained in

Section 3.4. On the other hand, the modulation amplitude is defined as:

$$\Delta\lambda_j^{(1)} = \left| \overline{\delta_{1,3j}^{\text{dip}}} - \overline{\delta_{1,3j}^{\text{max}}} \right|, \quad (41)$$

where $\overline{\delta_{1,3j}^{\text{dip}}}$ is the time average of function $\delta_1(t)$ at the three adjacent dips ($3j + 1$), ($3j + 2$) and ($3j + 3$), as indicated in the upper inset of Fig. 6. Similarly, $\overline{\delta_{1,3j}^{\text{max}}}$ is the time average of function $\delta_1(t)$ at its ($3j + 1$)-th, ($3j + 2$)-th and ($3j + 3$)-th maxima, which occur when the translation stage rests around the original position $x = 0$. The ratio between the amplitude modulation and the strain gives the sensitivity $S^{(1)}$ of FBG #1:

$$S^{(1)} = \frac{\partial\Delta\lambda^{(1)}}{\partial\varepsilon^{(1)}}. \quad (42)$$

By fitting a straight line to the data points $(\Delta\lambda_j^{(1)}, \varepsilon_j^{(1)})$, we retrieved $S^{(1)} = 1.217 \pm 0.006$ pm/ μ strain, which agrees with the nominal sensitivity of 1.2 pm/ μ strain provided by the manufacturer (Technicasa, T10). The minimum retrieved strain is 365 nanostrain and the corresponding minimum modulation amplitude obtained is $\Delta\lambda_{\text{min}} = 400 \pm 200$ fm. This value is more than two orders of magnitude smaller than the resolution of the FT spectrometer (50 pm). The value of $\Delta\lambda_{\text{min}}$, experimentally retrieved, is not limited by the resolution the FT spectrometer but only by the SNR of the input signal.

FBG #4 has been taken as a reference sensor and no external excitation is applied to it after the end of the calibration. However, for $t < 10$ s, Fig. 5(e) shows small fluctuations of function $\delta_4(t)'$ (of the order of a few pm), caused by the cross-talk among sensors. Since the modulation amplitude of FBG #1 is the larger for $t < 10$ s, its cross-talk with FBG #4 is dominant. The maximum cross talk between FBGs #4 and FBGs #1 is about 1% of the $\delta_1(t)$ value, which is acceptable in most applications.

In order to demonstrate the compensation of the thermal drift of the phases Ψ_m ($m = 1, \dots, M$), the chip is heated up using a Peltier element (MCPE1-03108NC-S 18.8W, Multicomp) placed a few centimeters above it. The Peltier hot surface reaches a temperature of 45 °C causing a shift of 35 pm to the solutions $\delta_1(t)'$, $\delta_2(t)'$, $\delta_3(t)'$ and $\delta_4(t)'$. The drift of $\delta_4(t)'$ can be observed in Fig. 5(e) for $t > 73$ s. Using Eq. (39) we calculated $\delta_1(t)$, $\delta_2(t)$ and $\delta_3(t)'$, where 92.0% of the phase drift has been compensated. Fig. 5(f) shows a comparison between $\delta_1(t)'$ and $\delta_1(t)$ while Figs. 5(c) and 5(d) show only the compensated solutions $\delta_2(t)$ and $\delta_3(t)$. For the sensors presented here, the phase drift could have been removed by applying a high pass filter to $\delta_1(t)'$, $\delta_2(t)'$ and $\delta_3(t)'$. However, for low speed sensors such as biochemical sensors [4], filtering is not possible since the speed of the sensor is comparable to the phase drift speed.

Although the method can be applied to high speed sensors, its real time implementation is challenging. On one hand, the speed of the FT spectrometer is limited only by the electronics and the integrated photodetectors may respond at frequencies higher than 5 GHz. On the other hand, a system of non-linear equations need to be solved at each instant of time. The computational costs, however, can be reduced by calculating the inverse of the Jacobian $\partial\hat{V}_m/\partial\delta_k$ analytically. Using the transformation $z_k(t) = 2\pi(\lambda_k(0) + \delta_k(t))/F_1$, it can be shown that the Jacobian is given by a product of a diagonal matrix and the Vandermond matrix $V(z_k)$. Since analytic expressions do exist [27] for the inverse of $V(z_k)$, the computational time is mainly governed by the time of calculating product of matrices. Moreover, the reduced number of interactions of Newton's method also contributes in reducing the computational time. Nevertheless, the real time interrogation of high speed sensors may require the usage of an application specific computational solution.

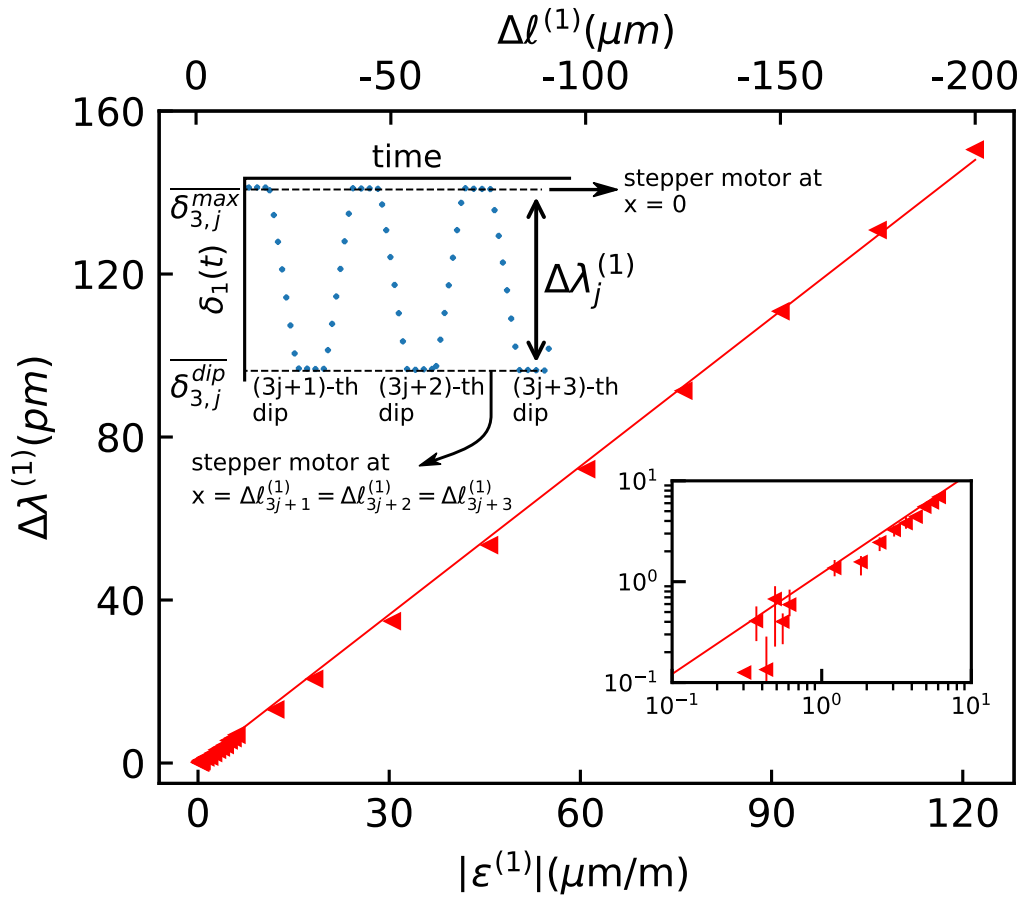


Fig. 6. Modulation amplitude $\Delta\lambda^{(1)}$ of sensor 1 as a function of the strain applied. $\Delta\lambda^{(1)}$ is calculated from as $\Delta\lambda^{(1)} = \left| \overline{\delta_{1,3j}^{dip}} - \overline{\delta_{1,3j}^{max}} \right|$, where $\overline{\delta_{1,3j}^{dip}}$ and $\overline{\delta_{1,3j}^{max}}$ are defined in upper inset of the fig. A straight line has been fitted to the data points $(|\varepsilon_j^{(1)}|, \Delta\lambda_j^{(1)})$. The slope, whose value is 1.217 ± 0.006 pm/microstrain, gives the sensitivity of FBG #1. The inset in the bottom of the fig. shows the data points $(\varepsilon_j^{(1)}, \Delta\lambda_j^{(1)})$ and the straight line fitted in a Loglog plot. The minimum amplitude modulation retrieved is 400 ± 200 pm.

5. Conclusion

A novel interrogation method based on FT spectroscopy is presented. The technique is promising due to its high flexibility, high sensitivity and reduced interrogator footprint. It can be applied in different situations, in particular, for arrays of integrated sensors where the resonance wavelengths cannot be predicted during the design stage. Three conditions have been identified for the proper interrogation of the sensors: (a) the number of interferometers must only be at least as large as the number of sensors, allowing the interrogator footprint to be relatively small; (b) the MZIs must have different OPDs; (c) the phases $2\pi\lambda_k(t)/F_1$ (for $k = 1, \dots, K$) needs to be different at any time. If the maximum amplitude modulation of the sensors is known, condition (c) is usually not an issue for FBG sensors, since the Bragg wavelengths could be chosen with an accuracy better than 1.0 nm. In case of integrated ring resonators, it is possible in most situations to design rings with a slightly different lengths, assuring a similar free spectral range, but different resonances.

Since the phases depend on F_1 , the proper design of the FT spectrometer gives an extra flexibility to avoid the phases $2\pi\lambda_k(t)/F_1$ to overlap.

It has been shown that the minimum modulation amplitude experimentally retrieved is not limited by resolution of the FT spectrometer, but limited only by the signal-to-noise ratio of the input signal. The minimum modulation amplitude obtained is 400 ± 200 fm and the cross-talk, which also depends on the SNR, is about 1%. Moreover, the phase drift of the interrogator, caused by temperature fluctuations, can be compensated by using one of the sensors as reference sensor to which no external excitation is applied. This is important for low speed sensors where the thermal induced drift of MZI phases is comparable to the speed of the sensors. Our method can also be applied for high speed sensors, but the implementation of real time interrogators require the analytic calculation of the inverse of the Jacobian matrix used in Newton's method. For real time interrogation the usage of application specific computational solutions may be needed.

Funding

Brazilian Council for Scientific and Technological Development (CNPq) (248560/2013-1).

Acknowledgments

We thank Smart Photonics for fabricating the InP chips and COBRA for providing the design of advanced waveguides. We also thank Optocap and Alter Technology Group for performing the wire bonding of our chips to the PCB.

References

1. F. G. Peternella, B. Ouyang, R. Horsten, M. Haverdings, P. Kat, and J. Caro, "Interrogation of a ring-resonator ultrasound sensor using a fiber mach-zehnder interferometer," *Opt. Express* **25**, 31622–31639 (2017).
2. C. Zhang, S. L. Chen, T. L. Ling, and L. J. Guo, "Imprinted polymer microrings as high performance ultrasound detectors in photoacoustic imaging," *J. Light. Technol.* **33**, 4318–4328 (2015).
3. E. Hallynck and P. Bienstman, "Integrated optical pressure sensors in silicon-on-insulator," *IEEE Photonics J.* **4**, 443–450 (2012).
4. K. de Vos, J. Girones, S. Popelka, E. Schacht, R. Baets, and P. Bienstman, "SOI optical microring resonator with poly (ethylene glycol) polymer brush for label-free biosensor applications," *Biosens. Bioelectron.* **24**, 2528–2533 (2009).
5. X. Zhou, Y. Dai, J. M. Karanja, F. Liu, and M. Yang, "Microstructured FBG hydrogen sensor based on pt-loaded waveguide," *Opt. Express* **25**, 8777–8786 (2017).
6. Q. Liang, K. Zou, J. Long, J. Jin, D. Zhang, G. Coppola, W. Sun, Y. Wang, and Y. Ge, "Multi-component FBG-based force sensing systems by comparison with other sensing technologies : A review," *IEEE Sensors J.* **18**, 7345–7357 (2018).
7. A. D. Kersey, "A review of recent developments in fiber optic sensor technology," *Opt. Fiber Technol.* **2**, 291–317 (1996).
8. H. Li, X. Ma, B. Cui, Y. Wang, C. Zhang, J. Zhao, Z. Zhang, C. Tang, and E. Li, "Chip-scale demonstration of hybrid III - V / silicon photonic integration for an FBG interrogator," *Optica* **4**, 692–700 (2017).
9. D. Pustakhod, E. Kleijn, K. Williams, and X. Leijtens, "High-resolution awg-based fiber," *IEEE Sensors J.* **28**, 2203–2206 (2016).
10. N. A. Yebo, W. Bogaerts, Z. Hens, and R. Baets, "On-chip arrayed waveguide grating interrogated silicon-on-insulator microring resonator-based gas sensor," *IEEE Photonics Technol. Lett.* **23**, 1505–1507 (2011).
11. H. Guo, G. Xiao, N. Mrad, and J. Yao, "Echelle diffractive grating based wavelength interrogator for potential aerospace applications," *J. Light. Technol.* **31**, 2099–2105 (2013).
12. U. Tiwari, K. Thyagarajan, M. R. Shenoy, and S. C. Jain, "EDF-based edge-filter interrogation scheme for FBG sensors," *IEEE Sensors J.* **13**, 1315–1319 (2013).
13. V. M. N. Passaro, A. V. Tsarev, and F. De Leonadis, "Wavelength interrogator for optical sensors based on a novel thermo-optic tunable filter in SOI," *J. Light. Technol.* **30**, 2143–2150 (2012).
14. P. Orr and P. Niewczas, "High-speed, solid state, interferometric interrogator and multiplexer for fiber Bragg grating sensors," *J. Light. Technol.* **29**, 3387–3392 (2011).
15. M. Perry, P. Orr, P. Niewczas, and M. Johnston, "High-speed interferometric fbg interrogator with dynamic and absolute wavelength measurement capability," *J. Light. Technol.* **31**, 2897–2903 (2013).
16. M. A. Davis and A. D. Kersey, "Application of a fiber fourier transform spectrometer to the detection of wavelength-encoded signals from bragg grating sensors," *J. Light. Technol.* **13**, 1289–1295 (1995).

17. K. B. Rochford and S. D. Dyer, "Demultiplexing of interferometrically interrogated fiber Bragg grating sensors using Hilbert transform processing," *J. Light. Technol.* **17**, 831–836 (1999).
18. M. Florjańczyk, P. Cheben, S. Janz, A. Scott, B. Solheim, and D. X. Xu, "Multiaperture planar waveguide spectrometer formed by arrayed Mach-zehnder interferometers," *Opt. express* **15**, 18176–18189 (2007).
19. K. Okamoto, H. Aoyagi, and K. Takada, "Fabrication of Fourier-transform, integrated-optic spatial heterodyne spectrometer on silica-based planar waveguide." *Opt. letters* **35**, 2103–2105 (2010).
20. A. V. Velasco, P. Cheben, P. J. Bock, A. Delâge, J. H. Schmid, J. Lapointe, S. Janz, M. L. Calvo, D. X. Xu, M. Florjańczyk, and M. Vachon, "High-resolution fourier-transform spectrometer chip with microphotonic silicon spiral waveguides," *Opt. letters* **38**, 706–708 (2013).
21. H. Podmore, A. Scott, P. Cheben, A. V. Velasco, J. H. Schmid, M. Vachon, and R. Lee, "Demonstration of a compressive-sensing fourier-transform on-chip spectrometer," *Opt. letters* **42**, 1440–1443 (2017).
22. A. Herrero-Bermello, A. V. Velasco, H. Podmore, P. Cheben, J. H. Schmid, S. Jans, M. L. Calvo, D.-X. Xu, A. Scott, and P. Corredera, "Temperature dependence mitigation in stationary Fourier-transform on-chip spectrometers," *Opt. letters* **42**, 2239–2242 (2017).
23. D. M. Kita, B. Miranda, D. Favela, D. Bono, J. Michon, H. Lin, T. Gu, and J. Hu, "High-performance and scalable on-chip digital fourier transform spectroscopy," *Nat. Commun.* **9**, 4405 (2018).
24. R. Uda, K. Yamaguchi, K. Takada, and K. Okamoto, "Fabrication of a silica-based complex fourier- transform integrated-optic spatial heterodyne spectrometer incorporating 120°optical hybrid couplers," *Appl. Opt.* **57**, 3781–3787 (2018).
25. K. Okamoto, "Fourier-transform, integrated-optic spatial heterodyne (fish) spectrometers on planar lightwave circuits," in *International Conference on Fibre Optics and Photonics*, (Optical Society of America, 2012), p. M2A.1.
26. A. Dandridge, "Fiber optic sensors based on the Mach-zehnder and michelson interferometers," in *Fiber Optic Sensors: an Introduction for engineers and scientists*, E. Udd and W. B. S. Jr., eds. (John Wiley and Sons, Inc., 1991), pp. 231–275.
27. F. Soto-Eguibar and H. Moya-Cessa, "Inverse of the Vandermonde and Vandermonde confluent matrices," *Appl. Math. Inf. Sci.* **5**, 361–366 (2011).